Broadband antireflection and light-trapping enhancement of plasmonic solar cells

Ren-Hao Fan,[1] Li-Hao Zhu,[1] Ru-Wen Peng,[1,*] Xian-Rong Huang,[2,†] Dong-Xiang Qi,[1]
Xiao-Ping Ren,[1] Qing Hu,[1] and Mu Wang[1,‡]
[1]*National Laboratory of Solid State Microstructures and Department of Physics, Nanjing University, Nanjing 210093, China*
[2]*Advanced Photon Source, Argonne National Laboratory, Argonne, Illinois 60439, USA*
(Received 12 December 2012; revised manuscript received 7 May 2013; published 30 May 2013)

In this work, we demonstrate broadband extraordinary transmission and antireflection in two-dimensional periodic metallic cuboids at optical frequencies. These phenomena originate from nonresonant excitations of surface plasmons, and represent high antireflection simultaneously for a broad spectral band and a wide angular range of incidence with polarization insensitivity. Based on this principle, we further introduce such metallic cuboids arrays into silicon solar cells. It is shown that high performance of light trapping in the cells can be achieved with a significant enhancement of the ultimate quantum efficiency. This study shows promising applications of plasmonic nanostructures to high-efficiency photovoltaic devices.

DOI: 10.1103/PhysRevB.87.195444 PACS number(s): 42.25.Bs, 78.67.−n, 88.40.−j

I. INTRODUCTION

Enhancing the efficiency of solar cells has been of great interest in recent years. In general, there are three basic requirements for solar cells to achieve high efficiency.[1–4] First, the cell surface must be highly antireflective for the broadband solar spectrum over a wide angular range such that the solar energy can be sufficiently absorbed and trapped in the cell. Second, the absorbed energy must efficiently produce photocarriers instead of generating heat or other effects. Third, the solar cells should also have high conductivity for the photocarriers to be effectively collected with minimum combination in the bulk.

Flat and homogenous metallic films are generally extremely reflective to light, although they satisfy the high-conductivity requirement of solar cells. However, from intense studies in recent decades, nanostructured metallic films have been demonstrated to have completely different properties. Such metallic nanostructures can support surface plasmons (SPs) (i.e., excitations of collective conduction-electron waves at the interface between a metal and a dielectric[5]) or spoof surface plasmons[6] in the long-wavelength regime. A typical effect of the SP excitations is that they may lead to extraordinarily enhanced optical transmission through metallic films with significantly reduced reflection.[7–9] Meanwhile, SPs can trap and confine light in dimensions much smaller than the wavelength near the metal/dielectric interface, which may greatly enhance the interaction of light with thin active dielectric (or semiconductor) layers. Therefore, properly engineered metal/dielectric nanostructures in principle can meet all the above three requirements for making ultrahigh-efficiency thin-film solar photovoltaic (PV) devices.[10–14]

Nevertheless, one of the drawbacks of SP excitations is the inherently narrow bandwidth of operation, which is directly associated with the plasmonic resonance mechanisms.[7–9] Very recently, it was found both theoretically and experimentally that simple metallic gratings consisting of narrow slits can become transparent and completely antireflective for extremely broad bandwidths under oblique incidence.[15–18] This unnatural and fascinating phenomenon can be explained either by the nonresonant excitation mechanism of SPs and SSPs,[15] or by the anomalous impedance match between the grating and free space (or dielectric material) at the plasmonic Brewster angle.[16] One of the various potential applications of the ultrabroadband transmission mechanism is to make long-dreamed-of transparent metals.[15,17,19–22] But, for applications to antireflective photovoltaic devices, one-dimensional (1D) metallic gratings will suffer from two limitations. First, perfect ultrabroadband transmission can be achieved only for transverse-magnetic (TM) polarization while transverse-electric (TE) polarization is almost completely reflected.[23] Second, even for the TM polarization, high ultrabroadband transmission occurs only within a narrow angular range of extremely inclined incidence.

In this paper, we extend the principles of ultrabroadband transmission through 1D metallic gratings to 2D cases for both TM and TE waves. The 2D structures are periodic metallic cuboids on dielectric or semiconductor substrates. Note that, in the literature, 2D subwavelength hole arrays perforated in metallic films have been widely used to study extraordinary optical transmission phenomenon,[7,9,24] but the *absolute* transmission of these structures is usually very low. One of the reasons is that the waveguide modes in the holes have a cutoff frequency below which the wave fields inside the holes are evanescent. By contrast, the cuboid structures do not have this limitation. Therefore, here we demonstrate that such structures can achieve polarization-insensitive high transmission and antireflection simultaneously for a broad spectral band at optical frequencies and a wide angular range of incidence. Furthermore, by applying the periodic metallic cuboids as a broadband antireflection coating layer on silicon solar cells, we show that high performance of light trapping in the cells can be achieved with significant enhancement of the ultimate quantum efficiency. The investigation presents promising applications of plasmonic nanostructures to high-efficiency photovoltaic devices.

The paper is organized as follows. In Sec. II, we first show the experimental demonstration of broadband transmission for both TM and TE waves in 2D metallic cuboids in the optical frequency range. The experimental measurements agree reasonably well with numerical calculations based on the finite-difference time-domain method. A nonresonant feature has also been explored that depends on the spatial

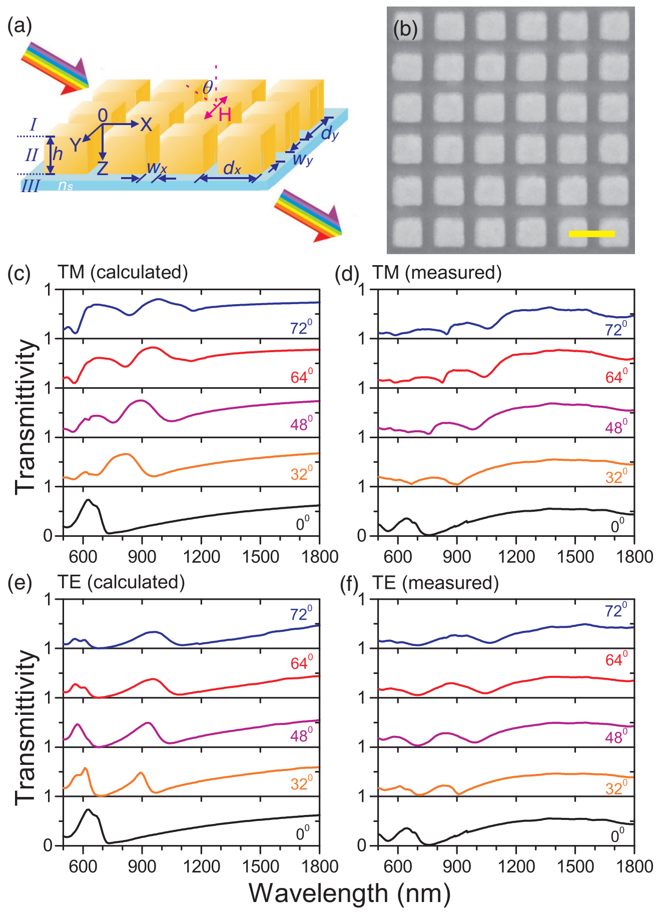

FIG. 1. (Color online) (a) Schematic of metallic cuboids on a glass substrate. (b) SEM image of the sample, $d_x = d_y = 450$ nm, $w_x = w_y = 150$ nm, $h = 100$ nm, and $n_s = 1.47$. The scale bar is 500 nm. The transmission spectra at different incidence angles: (c) calculated spectra for TM polarization, (d) measured spectra for TM polarization, (e) calculated spectra for TE polarization, and (f) measured spectra for TE polarization.

distribution of electric fields. Then an analytical analysis of broadband antireflection in 2D metallic cuboids is described in Sec. III. Based on this principle, we further introduce such metallic cuboids arrays into silicon solar cells, and show high-performance light trapping in the cells. The ultimate quantum efficiency for this plasmonic solar cell is evaluated in Sec. IV. Further, the efficiency comparison between this plasmonic solar cell and the traditional ones is presented in Sec. V. The advantage of this plasmonic approach is also discussed. Finally, a summary is given in Sec. VI.

II. EXPERIMENTAL AND NUMERICAL DEMONSTRATION OF BROADBAND TRANSMISSION IN 2D PERIODIC METALLIC CUBOIDS

First let us experimentally demonstrate high ultrabroadband transmission through 2D metallic cuboids in the optical frequency range. The 2D periodic metallic cuboids we studied are schematically shown in Fig. 1(a), where a TM or TE wave is incident on the structure at an angle θ to the Z axis. The period and the gap width along the X (Y) axis are d_x and w_x (d_y and w_y), respectively, and h is the thickness of the cuboids. The refractive index of the substrate is n_s. During the fabrication of the samples, we first coated a 100-nm-thick gold film on optical glass by magnetron sputtering. Then a focused-ion-beam facility (strata FIB 201, FEI company, with 30 keV Ga ions) was used to mill the cuboid structures. A microspectrophotometer (Craic, QDI2010) was used to measure the optical spectra of the samples. The numerical calculations are based on the finite-difference time-domain (FDTD) method[25] with Lumerical FDTD solution 8.0.1.

A field-emission scanning-electron microscope (SEM) image of one sample is shown in Fig. 1(b) with $d_x = d_y = 450$ nm, $w_x = w_y = 150$ nm, and $h = 100$ nm. The calculated and experimentally measured transmission spectra under different incidence angles are shown in Figs. 1(c)–1(f). More data for incidence angles from 0° to 72° can be found in Fig. A1 in the Supplemental Material.[26] When the incident wave is TM polarized [Figs. 1(c) and 1(d), with the magnetic field **H** parallel to the Y axis], the first-order Wood's anomaly along the X direction is $\lambda_{\mathrm{WD}x1}(\theta) = n_s d_x(1 + \sin\theta)$, which shifts from d to $2d$ with increasing θ. The transmittivity increases from $\theta = 0°$ (normal incidence) to $\theta = 64°$, and then slightly decreases when θ further increases towards 90°. In particular, the transmission spectra become nearly flat at $\theta = 64°$ for long wavelengths $\lambda > \lambda_{\mathrm{WD}x1}$, and the experimentally measured flat transmittivity is nearly 80%. Therefore, the high ultrabroadband transmission in 2D periodic metallic cuboids for $\lambda > \lambda_{\mathrm{WD}x1}$ is similar to that of 1D metallic gratings under oblique incidence.[15–17]

For TE polarization (with the electric field **E** parallel to the Y axis), significant transmission still occurs in Figs. 1(e) and 1(f) for long wavelengths $\lambda > \lambda_{\mathrm{WD}x1}$. This is different from the effect in 1D metallic gratings, where TE waves are almost completely reflected in the long-wavelength range. In Figs. 1(e) and 1(f), the transmission only slightly decreases with increasing θ from 0° to 90°, so high ultrabroadband transmission is achieved for both normal- and oblique-incidence configurations. Therefore, the 2D periodic metallic cuboids are largely transparent also for TE waves in a wide angular range. This is a remarkable advantage for applications to solar cells that require transmission and antireflection of both TM and TE waves.

For different ratios of w_x/d_x along the X axis, the maximum ultrabroadband transmission occurs around different optimal incident angles (θ_m). The calculated and measured θ-dependent TM transmission spectra with three different w_x/d_x ratios are shown in Fig. 2. The experimentally observed optimal angles are $\theta_m = 68°$ in Fig. 2(b) for $w_x/d_x = 0.25$, $\theta_m = 62°$ in Fig. 2(d) for $w_x/d_x = 0.375$, and $\theta_m = 56°$ in Fig. 2(f) for $w_x/d_x = 0.5$. Obviously, the angular range (area) of the incident angle corresponding to high ultrabroadband transmission broaden when the radio w_x/d_x increases. For small w_x/d_x, high transmission occurs only near the optimal angle, but under conditions such as $w_x/d_x = 0.5$, significant transmission is observed in a wider angular range. Thus, we have demonstrated that high transmission and low reflection of 2D metallic cuboids can be achieved for both broad spectral bands and wide angular ranges.

The phenomenon of high ultrabroadband transmission has a nonresonant feature, which can be understood from the $|\mathbf{E}|^2$ distribution. Figure 3(a) shows the calculated transmission

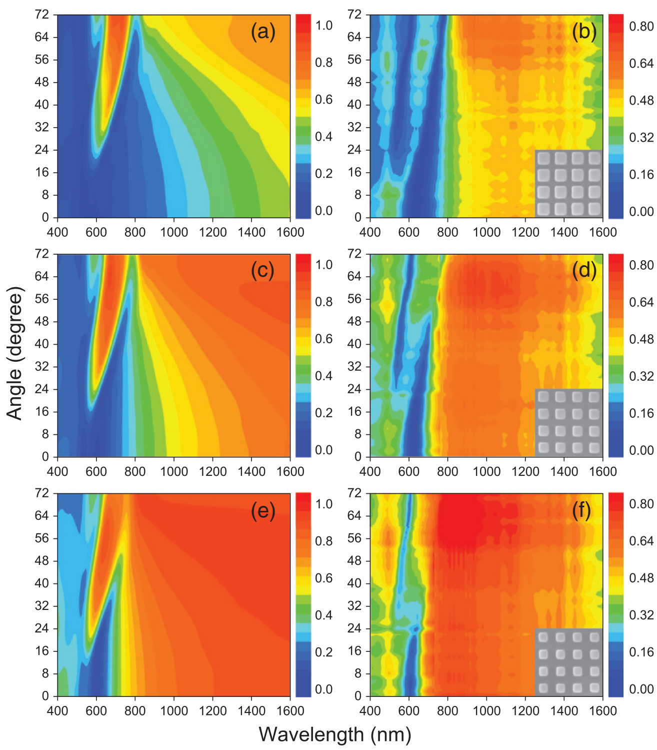

FIG. 2. (Color online) Calculated and experimentally measured angular transmission spectra, TM polarization. The color bar shows the transmission intensity. $d_x = d_y = 320$ nm, $h = 100$ nm, and $n_s = 1.47$. For the sample with $w_x = w_y = 80$ nm: (a) calculated spectra and (b) measured spectra. For the sample with $w_x = w_y = 120$ nm: (c) calculated spectra and (d) measured spectra. For the sample with $w_x = w_y = 160$ nm: (e) calculated spectra and (f) measured spectra. Insets show the SEM images of the corresponding samples.

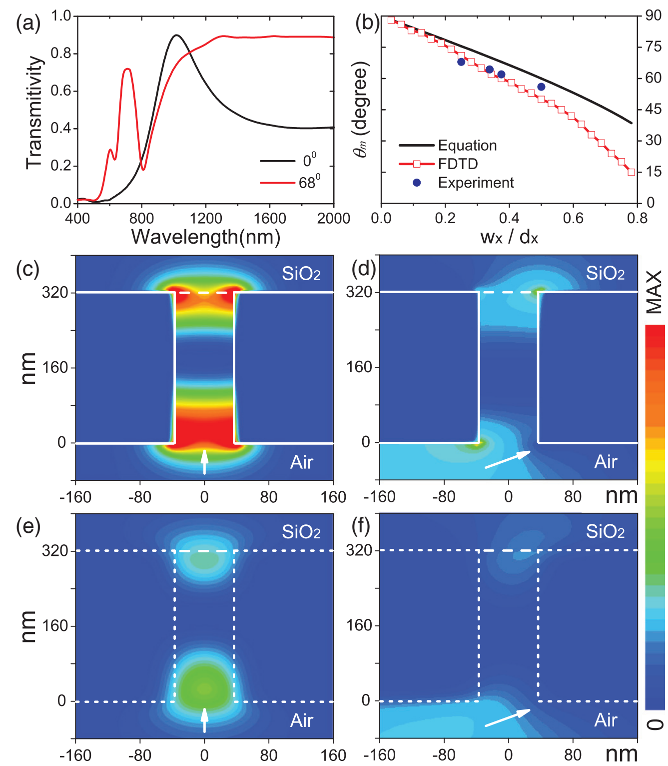

FIG. 3. (Color online) (a) Calculated transmission spectra under incidence of 0° and 68°, $d_x = d_y = 320$ nm, $w_x = w_y = 80$ nm, $h = 320$ nm, and $n_s = 1.47$. (b) Dependence of the optimal incident angle (θ_m) obtained by Eq. (2), FDTD simulations, and the experiments, respectively. The cross-sectional distribution of electric fields ($|\mathbf{E}|^2$) at the center of the cuboids ($y = 120$ nm): (c) $\theta = 0°$ at $\lambda = 1020$ nm, and (d) $\theta = 68°$ at $\lambda = 1600$ nm. The cross-sectional distribution of electric fields ($|\mathbf{E}|^2$) at the center of the slit ($y = 280$ nm): (e) $\theta = 0°$ at $\lambda = 1020$ nm, and (f) $\theta = 68°$ at $\lambda = 1600$ nm.

spectra of the sample under incidence angles of 0° and 68°, and the corresponding $|\mathbf{E}|^2$ fields are shown in Figs. 3(c)–3(f) at two specific wavelengths. For normal incidence, one can see that a Fabry-Pérot (FP) resonance peak appears at $\lambda = 1020$ nm. This wavelength satisfies $\lambda_N = 2h/N + \Delta_N$, where $N > 0$ is an integer and Δ_N is the redshift of the peak.[15,27–29] Since the FP peak is due to the resonance effect, we can see that the electric field shows a standing-wave pattern in Figs. 3(c) and 3(e). (This indicates that for normal incidence, one needs to use thin metal layers for solar cells to avoid FP resonance.) In contrast, under the oblique-incidence condition $\theta = 68°$, high and flat transmission appears for all the wavelengths $\lambda > 1200$ nm. As expected, the electric fields in Figs. 3(d) and 3(f) show a nonresonant feature since the $|\mathbf{E}|^2$ field intensity is much lower than that for the FP resonance. [Here the scale is the same in Figs. 3(c)–3(f) for comparison.] This nonresonant feature can reduce the loss from the metal layer.

III. ANALYTICAL ANALYSIS OF BROADBAND ANTIREFLECTION ON 2D PERIODIC METALLIC CUBOIDS

The phenomenon of high broadband transmission and antireflection for 2D periodic metallic cuboids can be understood from the detailed analytical solutions of Maxwell's equations in the Supplemental Material.[26] From these analyses, the reflection coefficient can be expressed as

$$r = \frac{\left(A - \frac{n_s \beta_s^2}{k_0^2 \cos^2\theta} B\right) \tan(\beta_s h) + i \frac{(n_s - 1)\beta_s}{k_0 \cos\theta} C}{\left(A + \frac{n_s \beta_s^2}{k_0^2 \cos^2\theta} B\right) \tan(\beta_s h) + i \frac{(n_s + 1)\beta_s}{k_0 \cos\theta} C}, \quad (1)$$

where

$$A = \begin{cases} 1 & \text{(for TM)}, \\ w_y^2/d_y^2 & \text{(for TE)}, \end{cases} \qquad B = \begin{cases} w_x^2/d_x^2 & \text{(for TM)}, \\ 1 & \text{(for TE)}, \end{cases}$$

$$C = \begin{cases} w_x/d_x & \text{(for TM)}, \\ w_y/d_y & \text{(for TE)}, \end{cases}$$

$k_0 = 2\pi/\lambda$, and β_s is the wave number in the slit. For TM polarization, the minimum reflection appears at $(\beta_s w_x)/(k_0 d_x \cos\theta) = 1$ or $\tan(\beta_s h) = 0$. Note that the FP resonance corresponds to $\tan(\beta_s h) = 0$. Therefore, the optimal incident angle for high ultrabroadband transmission and antireflection satisfies

$$\theta_m = \cos^{-1}[(\beta_s w_x)/(k_0 d_x)] \quad (2)$$

in 2D periodic metallic cuboids. In fact, when TM light is incident at the optimal angle (θ_m), the reflection coefficient reaches the minimum:

$$r_{\min} = \frac{(1 - n_s)\tan(\beta_s h) + i(n_s - 1)}{(1 + n_s)\tan(\beta_s h) + i(n_s + 1)}. \quad (3)$$

As indicated in Fig. 3(b), the θ_m calculated from Eq. (2) reasonably agrees with the simulated one from the FDTD method, particularly for the cases with low w_x/d_x. Most importantly, the experimentally measured results agree well with both the calculations for the FDTD method and the predictions from Eq. (2). All these results justify the current theory of the optimal angle for 2D periodic metallic cuboids. For TE polarization, the minimum reflection can be found at $\theta = 0$ or $\tan(\beta_s h) = 0$ (FP resonance). For $\lambda > d_y$, the reflection increases with increasing θ. However, if $\lambda \gg h$, extremely low reflection can be achieved for both TM and TE polarization states, indicating that polarization-insensitive antireflection can be achieved from 2D periodic metallic cuboids, especially in the long-wavelength range.

IV. BROADBAND LIGHT-TRAPPING ENHANCEMENT OF PLASMONIC SOLAR CELLS BASED ON 2D PERIODIC METALLIC CUBOIDS

In the following, we will demonstrate that 2D periodic metallic cuboids can be used to design broad-angle and ultrabroadband solar cells based on the above high-transmission and antireflection effects. Consider the structure of the solar cell in Fig. 4(a) that consists of three layers. On the top is a 2D periodic array of metallic cuboids made of (low-cost) aluminum. In the middle is a 20-nm-thick silicon oxide layer, below which is the semi-infinite single-crystalline silicon layer acting as the absorber.

In our design, the aluminum cuboids have the periods $d_x = d_y = 160$ nm, the gap widths $w_x = w_y = 80$ nm, and the thickness $h = 80$ nm. The silicon oxide layer is required in order to avoid additional surface combination,[1] since the dielectric spacer layer between the aluminum cuboids and the semiconductor can cause electrical isolation. The silicon oxide layer (20 nm) meanwhile offers a graded-index layer, which also reduces the reflection.[30] The absorbance[31] of the structure at a given wavelength (λ) is evaluated by $A(\lambda) = \omega \mathrm{Im}(\varepsilon) \int |E|^2 dV$, where $\mathrm{Im}(\varepsilon)$ is the imaginary part of the permittivity, ω and $\boldsymbol{E}$ are the angular frequency and electric field strength, respectively, and the integral is over the entire semi-infinite silicon layer.

The normalized absorbance in the semi-infinite single-crystalline silicon layer at different incident angles are shown in Figs. 4(b) and 4(c) for the TM and TE polarization states, respectively. For TE polarization, the absorbance decreases with increasing incidence angle, so the highest absorbance value is at 0°. For TM polarization, however, the absorbance increases with increasing incidence angle because of the high ultrabroadband transmission mechanisms discussed above. In addition, the reflection spectra of this solar cell are given in Figs. A2(a)–A2(b) in the Supplemental Material,[26] where the high antireflection of the solar cell can be observed. Because of the nonresonant feature of high transmission in the long-wavelength range, the loss from the metal layer is reduced, as indicated by the absorbance of the metal layer in Figs. A2(c)–A2(d) in the Supplemental Material.[26] Since the antireflection effect and nonresonant transmission both significantly reduce the loss from the metal layer, most of the light energy can be trapped in the active layer. Consequently,

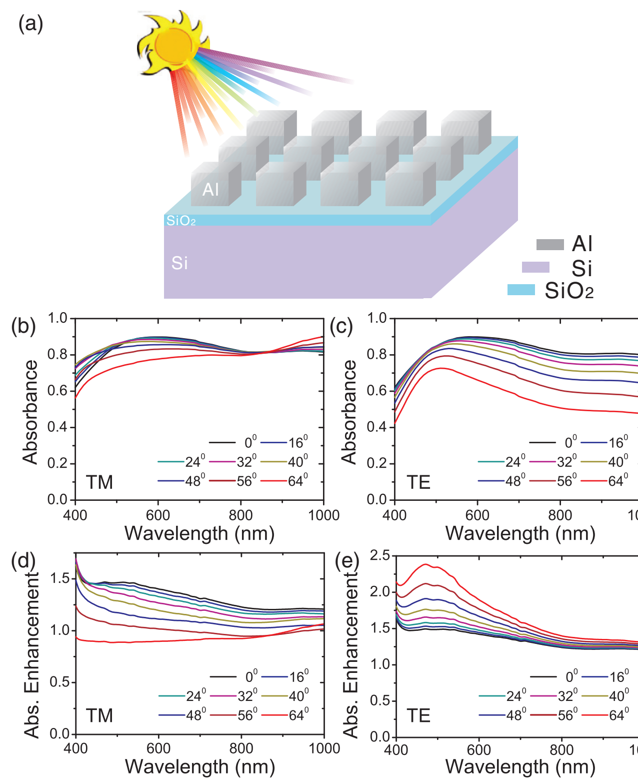

FIG. 4. (Color online) (a) Schematic of the plasmonic solar cell that consists of three layers. On the top is a 2D periodic array of metallic cuboids made of (low-cost) aluminum. In the middle is a 20-nm-thick silicon oxide layer, below which is the semi-infinite single-crystalline silicon layer acting as the absorber. Normalized absorbance in the silicon layer of this solar cell: (b) for TM polarization and (c) for TE polarization. The absorbance enhancement in the silicon layer of this solar cell: (d) for TM polarization and (e) for TE polarization. Here the parameters for this plasmonic solar cell are $d_x = d_y = 160$ nm, $w_x = w_y = 80$ nm, and $h = 80$ nm.

high absorbance in the semi-infinite single-crystalline silicon layer can be achieved.

It is worthwhile to discuss the absorbance enhancement of the present solar cell design, which can be defined by the factor $\Lambda(\lambda) = A(\lambda)/A_{\mathrm{ref}}(\lambda)$. Here $A(\lambda)$ is the absorbance of the silicon layer in this plasmonic solar cell, and $A_{\mathrm{ref}}(\lambda)$ is the absorbance of the same layer of silicon without adjacent coating, i.e., the naked silicon layer. The absorbance enhancement for both TM and TE polarization states at different incident angles is shown in Figs. 4(d) and 4(e). For TM polarization, most of the enhancement factors $\Lambda(\lambda)$ are greater than unity, which indicates high performance of light trapping in the active layer. It is also shown that the enhancement factors for TE polarization are even better than those for TM polarization.

To further demonstrate that the present design is suitable for high-performance solar cells, we calculate its ultimate quantum efficiency (QE),[31,32] which assumes that every absorbed photon with energy larger than the electronic band gap produces exactly one electron-hole pair. The ultimate QE then evaluates the fraction of the incident solar photons which are absorbed and converted to electron-hole pairs under the

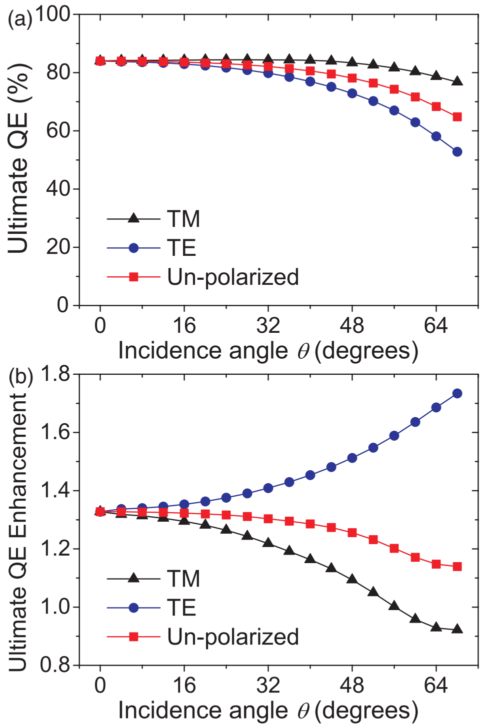

FIG. 5. (Color online) (a) The ultimate quantum efficiency (QE) of the plasmonic solar cell for different polarizations. (b) The ultimate QE enhancement for different polarizations. Here the parameters for the plasmonic solar cell are $d_x = d_y = 160$ nm, $w_x = w_y = 80$ nm, and $h = 80$ nm.

ideal process:[31,33]

$$QE = \frac{\int_{\lambda_1}^{\lambda_2} \frac{\lambda}{\hbar c} A(\lambda) I_{\mathrm{AM1.5G}}(\lambda) d\lambda}{\int_{\lambda_1}^{\lambda_2} \frac{\lambda}{\hbar c} I_{\mathrm{AM1.5G}}(\lambda) d\lambda}, \tag{4}$$

where λ is the incident wavelength, $\hbar$ is Plank's constant, c is the light speed in free space, and $I_{\mathrm{AM1.5G}}$ (λ) is the air mass 1.5 solar spectrum as usually adopted.[34] The ultimate QE in Fig. 5(a) is high within the wavelength range 400–1000 nm. For TM polarization, the ultimate QE is greater than 84% in a wide angular range, and it only slightly decreases when θ is above 56°. Here the ultimate QE value for TM polarization is better than that of TE polarization due to the higher normalized absorbance in the semi-infinite single-crystalline silicon layer. For the unpolarized situation, the ultimate QE remains around 80% in a wide angular range, which also corresponds to high efficiency of photon conversion into electron-hole pairs.

It is a common problem that the efficiency of solar cells usually depends on the incident angle.[1,35–37] To solve this problem, it is desirable to pursue omnidirecitional light absorption and trapping. Fortunately, the present plasmonic solar cell almost has this property. As shown in Fig. 5(b), its angle-dependent QE presents significant enhancement for all TM, TE, and unpolarized incident light. Obviously, most of the enhancement factors are greater than unity, indicating that the 2D periodic aluminum cuboids trap most of the photons into the solar cell rather than reflecting them back. Since solar light is unpolarized, we focus on the red curve in Fig. 5(b), which maintains a high enhancement factor around 1.3 for small-angle incidence (close to normal incidence). Even for large-angle incidence, the factor still exceeds 1.1. Therefore, high performance of the solar cell can be achieved for a wide angular range of incidence. If we assume that the incidence angle is from $\theta_1 = -68°$ to $\theta_2 = 68°$ for sunlight, the total quantum efficiency enhancement of the solar cell can be expressed as

$$QE_{\mathrm{EHM}} = \frac{\int_{\theta_1}^{\theta_2} QE(\theta)\cos\theta d\theta - \int_{\theta_1}^{\theta_2} QE_{\mathrm{ref}}(\theta)\cos\theta d\theta}{\int_{\theta_1}^{\theta_2} QE_{\mathrm{ref}}(\theta)\cos\theta d\theta} \times 100\%. \tag{5}$$

Our calculations based on this equation show that the current plasmonic solar cell can achieve an enhancement of the ultimate QE by about 29.5% due to the fact that 2D periodic metallic cuboids have the properties of wide-angle and broadband antireflection.

V. EFFICIENCY COMPARISON BETWEEN THE PLASMONIC SOLAR CELL AND TRADITIONAL SOLAR CELLS

It is well known that the traditional solar cells usually contain six parts. From bottom to top, they are the rear electrode, the back reflector, the active layer, the passivation layer, the top electrode, and the antireflection (AR) coating, respectively. For simplification, we ignore both the rear electrode and the back reflector, and consider only the other four parts, which play the following roles. (i) The active layer (such as the silicon layer) absorbs the sunlight and produces the photocarriers; (ii) the passivation layer efficiently reduces the surface recombination velocity and enhances the lifetime of the charge carriers; (iii) the top electrode collects the electrons and links to the external electrical circuit; and (iv) the AR coating, such as dielectric $\lambda/4$ AR coating,[38,39] is used to enhance the light absorption in the active layer. Nowadays, in high-performance photovaltaic devices, the standard c-Si surface passivation scheme uses thermal SiO_2 in order to yield outstanding characteristic.[40] Due to its long-term stability, SiN_x is also a good choice.[41] However, the top electrode, which is made of metallic material, suffers from its opaque covering and suppresses the solar energy coming into the device. For example, in a cell device[42] where a metal grid electrode of 20 μm width and 200 μm period is used, 10% of the solar energy is wasted due to the covering of the electrode.

The advantage of the present plasmonic solar cells is that 2D periodic metallic cuboids can combine the AR coating and the top electrode together, which inhibits the reflection of sunlight and reduces the loss caused by the previously used electrode covering at the same time. Actually, as shown in Figs. 6 and 7, the light trapping of this plasmonic solar cell is comparable with that of the traditional silicon solar cell using dielectric $\lambda/4$ AR coating. As we mentioned, the traditional solar cell uses $\lambda/4$ thick SiO_2 or SiN_x film as the AR coating [as shown in Figs. 6(a) and 6(b)]. For example, 100-nm-thick SiO_2 film or 70-nm-thick SiN_x film can significantly suppress the reflection of the light around the wavelength of 600 nm. (The refractive index of SiO_2 is taken as 1.47 and the refractive index of SiN_x as 2.1 in the

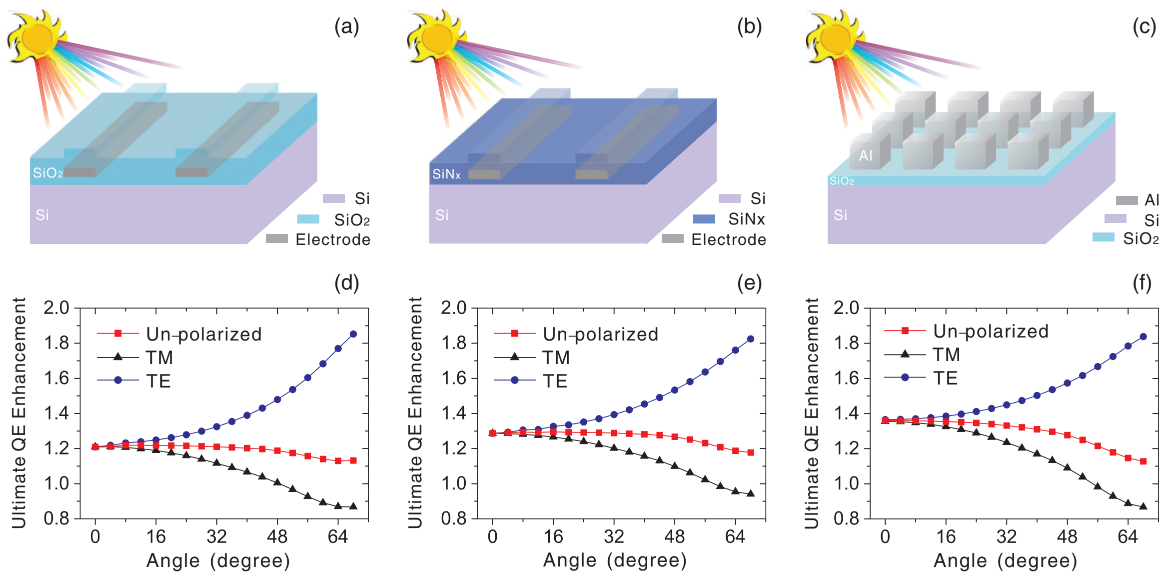

FIG. 6. (Color online) (a)Schematic and (d) ultimate QE enhancement of a solar cell containing a SiO_2 $\lambda/4$ AR coating and a metal grid electrode. (b)Schematic and (e) ultimate QE enhancement of a solar cell containing a SiN_x $\lambda/4$ AR coating and a metal grid electrode. (c)Schematic and (f) ultimate QE enhancement of the plasmonic solar cell based on 2D Al cuboids. The thickness of the SiO_2 AR coating in (a) is 100 nm, and the thickness of the SiN_x AR coating in(b)is 70 nm. The parameters of the 2D Al cuboids are $d_x = d_y = 120$ nm, $w_x = w_y = 60$ nm, and $h = 80$ nm and the thickness of the passivation layer (SiO_2) in (c) is 20 nm. The metal grid electrode accounts for 10% of the surface area.

calculation.) For a realistic comparison, the metal electrode should be taken into account and it covers about 10% of the surface area.[42] Then based on Eqs. (4) and (5), the ultimate QE enhancement of the silicon solar cells containing these two dielectric AR coatings can be evaluated, as shown in Figs. 6(d) and 6(e), respectively. As a result, the total QE enhancement of the cells can reach 20.2% for a SiO_2 AR coating and 27.7% for a SiN_x AR coating (as illustrated in Fig. 7). Interestingly, the total QE enhancement for the plasmonic solar cell can achieve 29.5%, which is slightly higher than for the traditional ones using dielectric AR coatings (see Fig. 7). It is common that optical resonances may happen in metallic structures, but they usually depend on the incident angle. Thanks to the nonresonance mechanism we mentioned in Sec. II, this plasmonic solar cell based on 2D periodic metallic cuboids is not sensitive to the incident angle, which is comparable with the traditional solar cell using dielectric $\lambda/4$ AR coating. In particular, if the incident angle is within the range of $\theta = 0°–45°$, the ultimate QE enhancement of the plasmonic solar cell is obviously higher than one made with SiO_2 or SiN_x AR coating. This feature originates from the fact that the 2D nanocuboids of metal can achieve polarization-insensitive high antireflection and light trapping simultaneously for a broad spectral band at optical frequencies and a wide angular range of incidence.

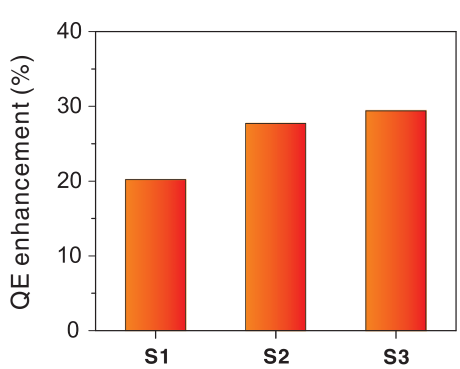

FIG. 7. (Color online) The total quantum efficiency enhancement of three types of silicon solar cells. S1 is the cell with 100-nm-thick SiO_2 AR coating; S2 is the cell with 70-nm-thick SiN_x AR coating; and S3 is the plasmonic solar cell with 2D Al cuboids, where $d_x = d_y = 120$ nm, $w_x = w_y = 60$ nm, and $h = 80$ nm, and the passivation layer is 20-nm-thick SiO_2.

VI. SUMMARY

In summary, we have demonstrated high ultrabroadband transmission and antireflection of 2D periodic metallic cuboids at optical frequencies for both TM and TE polarized light, and, accordingly, these plasmonic structures can make crystalline silicon achieve very efficient polarization-insensitive light trapping for a broad spectral band in a wide angular range of incidence. It has been verified that such 2D plasmonic structures can be used to design wide-angle and ultrabroadband silicon solar cells with significant enhancement of the ultimate quantum efficiency achievable. These mechanisms may be applied to improve the performance of various other photovoltaic devices.

ACKNOWLEDGMENTS

This work was supported by the Ministry of Science and Technology of China (Grants No. 2012CB921502 and No. 2010CB630705), the National Science Foundation of China (Grants No. 11034005, No. 61077023, No. 50972057, and No. 11021403), and partly by the Ministry of Education of

China (Grant No. 20100091110029). X.R.H. was supported by the US Department of Energy, Office of Science, Office of Basic Energy Sciences, under Contract No. DE-AC02-06CH11357.

*Author to whom correspondence should be addressed: rwpeng@nju.edu.cn
†xiahuang@aps.anl.gov
‡muwang@nju.edu.cn

[1] H. A. Atwater and A. Polman, Nat. Mater. **9**, 205 (2010).
[2] T. Saga, NPG Asia Mater. **2**, 96 (2010).
[3] M. A. Green and S. Pillai, Nat. Photonics **6**, 130 (2012).
[4] M. Graetzel, R. A. J. Janssen, D. B. Mitzi, and E. H. Sargent, Nature (London) **488**, 304 (2012).
[5] W. L. Barnes, A. Dereux, and T. W. Ebbesen, Nature (London) **424**, 824 (2003).
[6] J. B. Pendry, L. Martin-Moreno, and F. J. Garcia-Vidal, Science **305**, 847 (2004).
[7] T. W. Ebbesen, H. J. Lezec, H. F. Ghaemi, T. Thio, and P. A. Wolff, Nature (London) **391**, 667 (1998).
[8] J. A. Porto, F. J. García-Vidal, and J. B. Pendry, Phys. Rev. Lett. **83**, 2845 (1999).
[9] H. Liu and P. Lalanne, Nature (London) **452**, 728 (2008).
[10] A. Shah, P. Torres, R. Tscharner, N. Wyrsch, and H. Keppner, Science **285**, 692 (1999).
[11] R. A. Pala, J. White, E. Barnard, J. Liu, and M. L. Brongersma, Adv. Mater. **21**, 3504 (2009).
[12] F. J. Tsai, J. Y. Wang, J. J. Huang, Y. W. Kiang, and C. C. Yang, Opt. Express **18**, A207 (2010).
[13] U. W. Paetzold, E. Moulin, B. E. Pieters, R. Carius, and U. Rau, Opt. Express **19**, A1219 (2011).
[14] A. Niv, M. Gharghi, C. Gladden, O. D. Miller, and X. Zhang, Phys. Rev. Lett. **109**, 138701 (2012).
[15] X. R. Huang, R. W. Peng, and R. H. Fan, Phys. Rev. Lett. **105**, 243901 (2010).
[16] A. Alù, G. D'Aguanno, N. Mattiucci, and M. J. Bloemer, Phys. Rev. Lett. **106**, 123902 (2011).
[17] R. H. Fan, R. W. Peng, X. R. Huang, J. Li, Y. Liu, Q. Hu, M. Wang, and X. Zhang, Adv. Mater. **24**, 1980 (2012).
[18] N. Aközbek, N. Mattiucci, D. de Ceglia, R. Trimm, A. Alù, G. D'Aguanno, M. A. Vincenti, M. Scalora, and M. J. Bloemer, Phys. Rev. B **85**, 025430 (2012).
[19] I. R. Hooper, T. W. Preist, and J. R. Sambles, Phys. Rev. Lett. **97**, 053902 (2006).
[20] G. Subramania, S. Foteinopoulou, and I. Brener, Phys. Rev. Lett. **107**, 163902 (2011).
[21] J. T. Shen, P. B. Catrysse, and S. Fan, Phys. Rev. Lett. **94**, 197401 (2005).
[22] P. Yeh, Opt. Commun. **26**, 289 (1978).
[23] K. Kawano and T. Kitoh, *Introduction to Optical Wave-guide Analysis* (John Wiley & Sons, New York, 2001).
[24] Z. H. Tang, R. W. Peng, Z. Wang, X. Wu, Y. J. Bao, Q. J. Wang, Z. J. Zhang, W. H. Sun, and Mu Wang, Phys. Rev. B **76**, 195405 (2007).
[25] A. Taflove and S. C. Hagness, *Computational Electrodynamics: The Finite-Difference Time-Domain Method*, 3rd ed. (Artech House, Norwood, MA, 2005).
[26] See Supplemental Material at http://link.aps.org/supplemental/10.1103/PhysRevB.87.195444 for detailed data from experiments, calculations and analytical solutions of the Maxwell equations.
[27] X. R. Huang and R. W. Peng, J. Opt. Soc. Am. A **27**, 718 (2010).
[28] H. E. Went, A. P. Hibbins, J. R. Sambles, C. R. Lawrence, and A. P. Crick, Appl. Phys. Lett. **77**, 2789 (2000).
[29] S. Collin, G. Vincent, R. Haïdar, N. Bardou, S. Rommeluère, and J. L. Pelouard, Phys. Rev. Lett. **104**, 027401 (2010).
[30] S. Chhajed, M. F. Schubert, J. K. Kim, and E. F. Schubert, Appl. Phys. Lett. **93**, 251108 (2008).
[31] W. Shockley and H. J. Queisser, J. Appl. Phys. **32**, 510 (1961).
[32] R. W. Peng, M. Mazzer, and K. W. J. Barnham, Appl. Phys. Lett. **83**, 770 (2003).
[33] B. C. P. Sturmberg, K. B. Dossou, L. C. Botten, A. A. Asatryan, C. G. Poulton, C. M. de Sterke, and R. C. McPhedran, Opt. Express **19**, A1067 (2011); L. H. Zhu, M. R. Shao, R. W. Peng, R. H. Fan, X. R. Huang, and Mu Wang, *ibid.* **21**, A313 (2013).
[34] ASTM, "Reference Solar Spectral Irradiance: Air Mass 1.5 Spectra," http://rredc.nrel.gov/solar/spectra/am1.5.
[35] S. Koynov, M. S. Brandt, and M. Stutzmann, Appl. Phys. Lett. **88**, 203107 (2006).
[36] V. E. Ferry, L. A. Sweatlock, D. Pacifici, and H. A. Atwater, Nano Lett. **8**, 4391 (2008).
[37] E. Verhagen, L. Kuipers, and A. Polman, Opt. Express **17**, 14586 (2009).
[38] B. S. Richards, Prog. Photovolt: Res. Appl. **12**, 253 (2004).
[39] M. L. Kuo, D. J. Poxson, Y. S. Kim, F. W. Mont, J. K. Kim, E. F. Schubert, and S. Y. Lin, Opt. Lett. **33**, 21 (2008).
[40] M. J. Kerr and A. Cuevas, Semicond. Sci. Technol. **17**, 35 (2002).
[41] S. Olibet, E. Vallat-Sauvain, and C. Ballif, Phys. Rev. B **76**, 035326 (2007).
[42] W. Kruehler and J. Grabmaier, US Patent No. 5,125,984 (1992).